Structure-Property Relations of Nanostructured Carbon Systems as a Function of Processing

by

Mackenzie E. Devoe

Submitted to the Department of Materials Science and Engineering
in partial fulfillment of the requirements for the degree of

Bachelor of Science in Materials Science and Engineering

at the

MASSACHUSETTS INSTITUTE OF TECHNOLOGY

June 2015

ARCHIVES
MASSACHUSETTS INSTITUTE OF TECHNOLOGY
JUN 08 2015
LIBRARIES

© Massachusetts Institute of Technology 2015. All rights reserved.

Author .... Signature redacted
Department of Materials Science and Engineering
May 1, 2015

Certified by .... Signature redacted ......
Brian L. Wardle
Associate Professor of Aeronautics and Astronautics
Thesis Supervisor

Certified by .... Signature redacted ....
Carl V. Tompson
Stavros Salapatas Professor of Materials Science and Engineering
Thesis Reader

Accepted by....... Signature redacted ....
Geoffrey Beach
Professor of Materials Science and Engineering
Chairman, Department Undergraduate Committee

Structure-Property Relations of Nanostructured Carbon Systems as a Function of Processing

by

Mackenzie E. Devoe

Submitted to the Department of Materials Science and Engineering
on May 1, 2015, in partial fulfillment of the
requirements for the degree of
Bachelor of Science in Materials Science and Engineering

Abstract

Due to their intrinsic properties and nanometer scale, carbon nanotubes (CNTs) are commonly used to enhance the material properties of engineering materials. However, structural defects can significantly alter the intrinsic properties of CNTs, thereby limiting the physical properties of aligned CNT nanocomposite architectures. Previous studies have shown the difficulty in getting quantitative data for CNT quality once embedded within a carbon matrix. Therefore, studies that focused on the CNTs and carbon matrix separately were necessary. A study on the CNTs and carbon matrix response to pyrolyzation temperatures has recently been completed and is used to inform and motivate the research reported here. This research will focus primarily on the effects of different temperature ramping rates (TRR's) during pyrolysis of phenolic resin to form the ceramic matrix. Preliminary X-Ray Diffraction (XRD), Raman spectroscopy and Vickers Hardness results indicate that increasing the temperature ramping rate (in the range of 10°C/min - 40°C/min) increases the prevalence of defects in the nanocomposite system as well as increasing the standard error of both crystallite sizes and hardness, while maintaining the mean of the distribution. Future studies exploring aligned CNT carbon matrix nanocomposites (A-CMNCs) and more extreme temperature ramping rates are proposed.

Thesis Supervisor: Brian L. Wardle
Title: Associate Professor of Aeronautics and Astronautics

Acknowledgements

I would like to thank Itai Stein for his guidance and support over the course of this and previous studies, as well as Hanna Vincent for my initial lab training and being a great student mentor. Thank you to Charles Settens for his advice and guidance in X-Ray Diffraction experimentation and analysis. Thanks to NECSTLab for their input, advice, and procurement of needed supplies. Thank you to Dale for volunteering on short notice to do a final read through and giving awesome final comments. Finally, I'd like to thank Professor Brian L. Wardle and Professor Carl V. Thompson for their guidance throughout.

Contents

Contents 7

1 Introduction 15

2 Theoretical Background 19

- 2.1 Curing and Pyrolysis 19
- 2.2 Analysis Methods 21
  - 2.2.1 Raman Spectroscopy 21
  - 2.2.2 Vickers Microhardness 23
  - 2.2.3 X-Ray Diffraction 24

3 Objectives and Approach 25

- 3.1 Objectives 25
- 3.2 Approach 25
  - 3.2.1 PyC Synthesis 26
  - 3.2.2 Morphology Characterization 26
  - 3.2.3 Mechanical Characterization 26

4 Processing and Experimental Procedures 29

- 4.1 PyC Synthesis 29
- 4.2 Density 30
- 4.3 X-Ray Diffraction (XRD) 30
- 4.4 Raman Spectroscopy 32
- 4.5 Vickers Hardness 34

5 Characterization **37**

5.1 Morphology Characterization 37

5.1.1 XRD Results/Discussion 37

5.1.2 Raman Spectroscopy Results/Discussion 39

5.2 Hardness 42

6 Conclusions and Recommendations **45**

6.1 Conclusions 45

6.2 Future Work 46

6.2.1 Curing and XRD 46

6.2.2 Vickers Hardness Testing 46

References **49**

List of Figures

1.1 Raman Spectrum of an as-grown CNT forest, pyrolytic carbon (PyC) baseline sample, and a $\sim$ 1 vol. % aligned CNT carbon matrix nanocomposite (CNT A-CMNC) sample showing that the CNT signal is dominated by the PyC signal in the $\sim$ 1 vol. % CNT A-CMNCs. 16

1.2 High resolution scanning electron micrographs of (a) a $\sim$ 1 vol. % CNT forest and (b) CNT A-CMNC. SEM images taken from Stein et al. paper[1] 16

1.3 Representative Raman Spectra of $\sim$ 4 vol. % densified CNT forests after up to two pyrolyzations indicating that pyrolysis does not change the general shape of the spectra.[2] 17

2.1 Schematic of (a) bonding of phenol and formaldehyde to form phenol formaldehyde, followed by (b) dehydration/curing reaction from heat to form crosslinking bonds, as presented by Kane and Mowrer.[3] 20

2.2 Schematic of possible dehydration reactions. (a) shows an intra-chain reaction, while (b) shows an inter-chain reaction, as presented by Jiang et al.[4] 21

2.3 Illustration of the previously proposed mechanism of graphite transformation into defected diamond consisting of three stages:[5,6] (1) graphite → nanocrystalline (NC) graphite; (2) NC graphite → amorphous carbon (a-C); (3) a-C → tetrahedral amorphous carbon (ta-C). (a) Position of the G band as a function of amorphization stage (sp^3) character demonstrating that the maximum G peak position occurs between stages 1 and 2. (b) Inverse of the ratio of the intensities of the G and D bands (I_G/I_D) illustrating that the minimum value of I_G/I_D occurs between stages 1 and 2. 22

2.4 Schematic of crystallite shape showing (a) Lc and (b) La Image from Li et al.[7] 24

4.1 Image of sample preparation process. (a) cured phenolic resin in silicon mold, (b) cured phenolic outside of mold and pieces cut down and ready for pyrolysis, (c) example of pyrolyzed phenolic resin (older sample of larger size), (d) pyrolyzed pieces covered with epoxy in silicon mold, and (e) epoxy mold taken out of silicon mold after polishing. 30

4.2 Image of (a) PANalytical X'Pert PRO XRPD and (b) a close up of the furnace attachment used. 31

4.3 Resultant XRD spectra of 20°C/min TRR. (a) Spectra with background. (b) Spectra without background. 200 peak seen at $\sim 23^\circ$ and 110 peak seen at $\sim 43^\circ$ 32

4.4 Image of Raman Machine. 32

4.5 Schematic of typical spectra with FWHMs shown in red, and areas used to calculate G/D ratio shaded. 34

4.6 Image of LECO Hardness Machine. 35

5.1 Plots of L_a and L_c values calculated from XRD analysis at varying temperature ramping rates. 38

5.2 Plots showing (a.) G-peak FWHM and (b.) D-peak FWHM change with respect to TRR with standard error bars. 40

5.3 Plots showing La change with respect to TRR with standard error bars. . . . 41

5.4 Plot showing evolution of $(I_{\mathrm{G}}/I_{\mathrm{D}})$ as a function of disorder. The maximum of the curve is representative of the transition between nanocrystalline graphite and amorphous carbons. Image taken from Ferrari et al. paper.[8] . 42
5.5 Plot showing density change with respect to TRR with standard/measured error bars. 43
5.6 Plots showing (a) Hardness and (b) Specific Hardness changes with respect to TRR with standard error bars. 44

List of Tables

5.1 L_a (Angstroms) values for increasing Tp at varying TRRs 38

5.2 Density values for varying TRRs with error calculations 43

Chapter 1

Introduction

The intrinsic physical properties and scale (*i.e.* their high surface area to volume ratio) of carbon nanotubes (CNTs) makes their architectures prime candidates for next-generation high value structures and devices.[9–12] Since this work focuses on high temperature, extreme environment applications, an attempt to study aligned CNT carbon matrix nanocomposites (A-CMNCs) fabricated from polymer matrix precursors via the typical synthesis routes of polymer derived ceramics is necessary.[13–16] The high processing temperatures associated with pyrolysis are hypothesized to influence the concentration, type, and morphology of the wall defects in the CNTs,[17,18] thus, an analysis of the quality of the CNTs before and after incorporation into the ceramic matrix must be performed.

Initial studies using Raman Spectroscopy (a very useful tool for studying defects in carbon materials[5,6,19,20]) to quantify the evolution of the G-band and D-band peaks (indicative of graphitic (sp^2) and diamond (sp^3) like bonding, respectively) of the Raman spectrum showed no difference between the A-CMNC and purely ceramic matric samples. Representative spectra of as-grown CNTs, the pyrolytic carbon (PyC) matrix, and an A-CMNC are shown in Fig. 1.1.

High resolution scanning electron micrograph of a $\sim$ 1 vol. % CNT forest and a CNT A-CMNC (Fig. 1.2), illustrate that the presence of the PyC matrix fewer CNTs at the CNT A-CMNC surface. Considering a laser spot size of about 10 μm, it can be concluded that the signal originating from the CNTs is not sufficient to significantly influence the A-CMNC spectrum, thereby preventing any damage caused to the CNT walls by pyrolysis

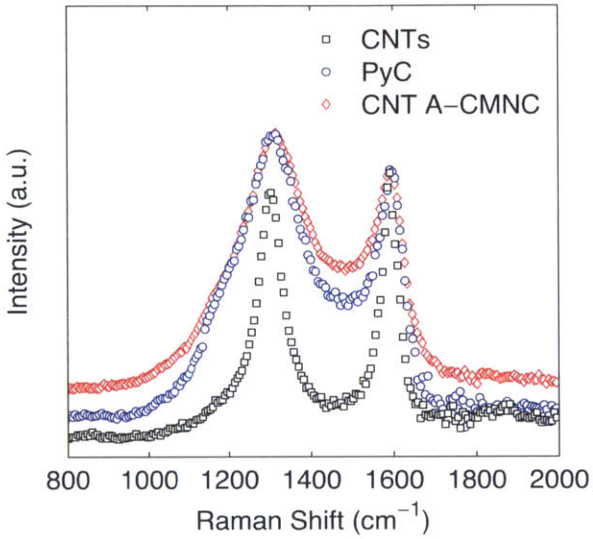

Figure 1.1: Raman Spectrum of an as-grown CNT forest, pyrolytic carbon (PyC) baseline sample, and a $\sim$ 1 vol. % aligned CNT carbon matrix nanocomposite (CNT A-CMNC) sample showing that the CNT signal is dominated by the PyC signal in the $\sim$ 1 vol. % CNT A-CMNCs.

from being quantified.

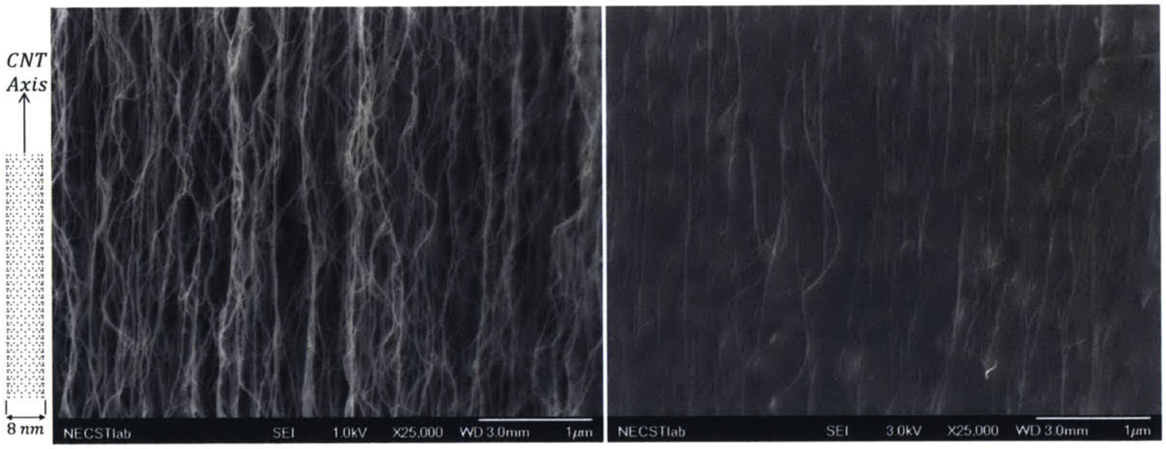
CNT
Axis
8 nm
NECSTlab SEI 1.0kV X25,000 WD 3.0mm 1μm
NECSTlab SEI 3.0kV X25,000 WD 3.0mm 1μm

Figure 1.2: High resolution scanning electron micrographs of (a) a $\sim$ 1 vol. % CNT forest and (b) CNT A-CMNC. SEM images taken from Stein et al. paper[1]

A separate study was carried out in response to this which focused on the effects of pyrolysis conditions on the as-grown CNTs alone. No significant change in peak position nor width was observed, showing there was insignificant damage to the CNTs, even after two cycles of the pyrolysis processing time and temperatures (see Fig. 1.3[2]).

Following this, it can be concluded that since the CNTs are not damaged due to pyroly-

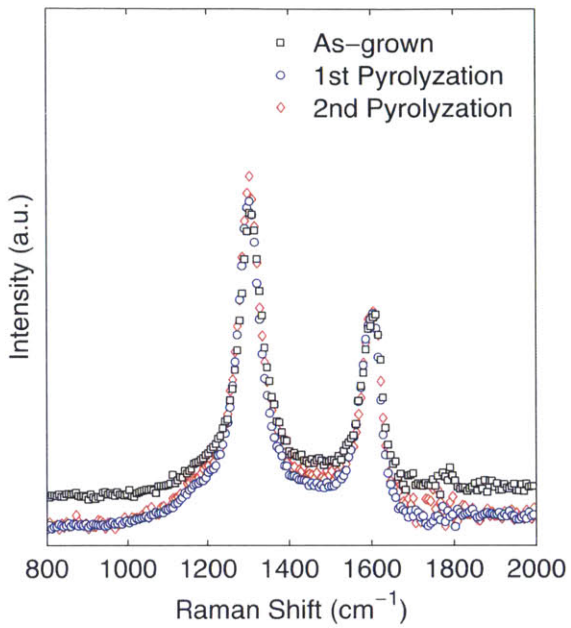

Figure 1.3: Representative Raman Spectra of ~ 4 vol. % densified CNT forests after up to two pyrolyzations indicating that pyrolysis does not change the general shape of the spectra.[2]

sis conditions, the properties of the pyrolytic carbon (PyC) matrix of the A-CMNCs likely dominate the Raman signal (and the stiffness of the nanocomposites), and that evaluation of the dependence of the structural behavior of the PyCs on processing is the first step towards quantification of the CNT reinforcement mechanism. This study will therefore focus on changes in structure/properties of the PyC in response to changes in the ramping rate to the pyrolysis temperature.

Chapter 2

Theoretical Background

This chapter will discuss the theory behind the curing of phenolic formaldehyde and the subsequent pyrolysis processing of the cured phenolic resin. Additionally, the theory behind Raman Spectroscopy and X-Ray Diffraction testing methods will be discussed.

2.1 Curing and Pyrolysis

Phenolic formaldehyde resin is formed from the reaction between phenol and formaldehyde. The type of phenolic resin used in this study was base-catalysed phenol-formaldehyde resin, meaning it has a formaldehyde to phenol ratio greater than one. This allows the resin to be cured without the use of a cross-linker. The resin polymerizes with heat, firstly forming hydroxymethyl and benzylic ether bonds, which amass at ~70°C and gives the material a thick, mostly solid state. Secondly, a further increase in temperature, typically to the range of 120°C - 150°C, dehydration of the material causes the breaking of some of the these ether bonds and formation stronger cross-linking bonds, that result in a harder state.[21] See Fig. 2.1 for a schematic of described reactions.

Pyrolysis occurs when an organic material decomposes due to high temperatures in an environment free of oxygen. The decomposition involves a change in the chemical composition as well as the physical phase. During this process, byproducts are released, the most significant according to literature research being: CO, CO_2, CH_4, and H_2O. The production of these gases correspond to different cross-linking reactions taking place.[22] Production

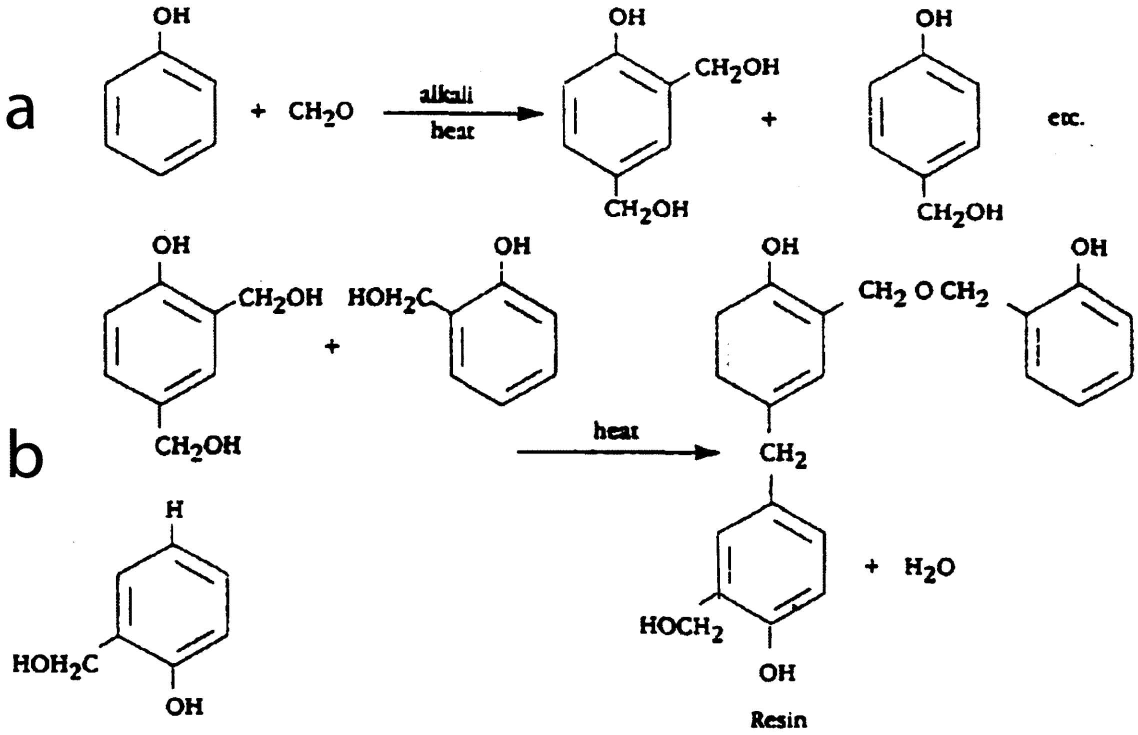
a
OH
+ CH_2O
alkali
heat
OH
CH_2OH
CH_2OH
+
OH
CH_2OH
etc.
b
OH
CH_2OH
CH_2OH
+
HOH_2C
OH
H
HOH_2C
OH
heat
OH
CH_2 O CH_2
OH
CH_2
$HOCH_2$
OH
+ H_2O
Resin

Figure 2.1: Schematic of (a) bonding of phenol and formaldehyde to form phenol formaldehyde, followed by (b) dehydration/curing reaction from heat to form cross-linking bonds, as presented by Kane and Mowrer.[3]

of CO occurs at two different stages in the pyrolysis, once before tar (tar: a dark, thick, flammable liquid that consists of hydrocarbons, resins, alcohols, and other compounds) starts to form around ~450°C, and the other after tar begins to form at ~620°C.

The formation of H_2O occurs after tar formation, increasing in frequency of formation with elevated temperatures and time at those temperatures, and is well-known to be associated with cross-linking reactions. H_2O can be a result of both inter-chain or intra-chain reactions as seen in Fig. 2.2.

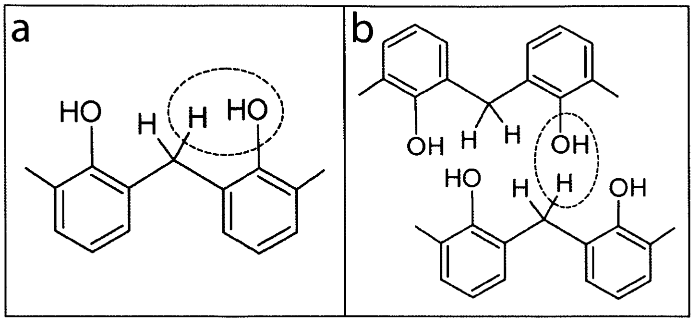

Figure 2.2: Schematic of possible dehydration reactions. (a) shows an intra-chain reaction, while (b) shows an inter-chain reaction, as presented by Jiang et al.[4]

2.2 Analysis Methods

2.2.1 Raman Spectroscopy

To study the structure of the PyCs, Raman spectroscopy, a non-destructive tool commonly used to study carbon materials,[5,6,19,20] was utilized.[1] Raman spectroscopy uses the inelastic scattering of monochromatic light to study the vibrational, rotational, and other low-frequency modes in a system. Since the re-emitted photons have lower energies than the incident photons, the inelastically scattered light also has a higher wavelength, and this difference is quantified by the Raman Shift[23]. For purposes of this study, the most important peaks are the G-mode and D-mode, both of which result from the inelastic backscatter of the incident laser light. In the case of PyCs, the D-peak is representative of sp^3 hybridized carbon and the G-band is representative of sp^2 hybridized carbon. It is important to note that the sp^2 carbon exhibit both σ (single) and π (double) bonds, while the sp^3 hybridized carbons only exhibit σ bonds. Since double bonds are stronger than single bonds, when incident light hits the bond, the double bonds are able to absorb more energy than the single bonds. Thus, the G-mode peak occurs at a larger Raman Shift value than the D-mode peak[24].

By comparing the intensity of the G-mode and D-mode peaks, referred to as the sample's G/D ratio, the quality of a PyC can be quantified. Unfortunately with increasing amounts of amorphous carbon, the G and D peak can broaden and overlap. Additionally, the spectra may have smaller peaks that overlap or add to the apparent G and D peaks.

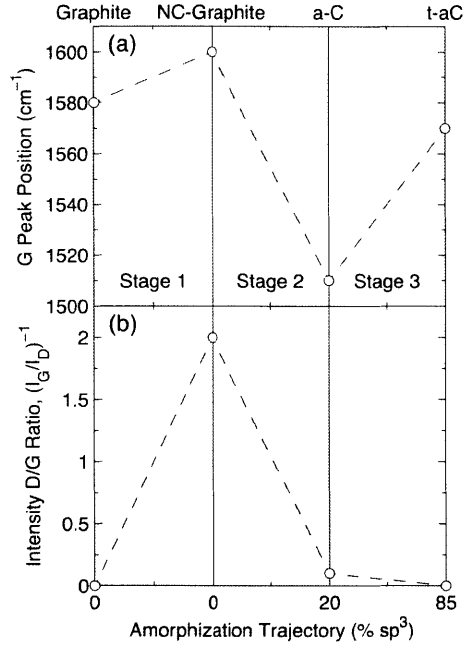

Figure 2.3: Illustration of the previously proposed mechanism of graphite transformation into defected diamond consisting of three stages:[5,6] (1) graphite → nanocrystalline (NC) graphite; (2) NC graphite → amorphous carbon (a-C); (3) a-C → tetrahedral amorphous carbon (ta-C). (a) Position of the G band as a function of amorphization stage (sp^3) character demonstrating that the maximum G peak position occurs between stages 1 and 2. (b) Inverse of the ratio of the intensities of the G and D bands (I_G/I_D) illustrating that the minimum value of I_G/I_D occurs between stages 1 and 2.

Literature suggests that the typical Raman spectrum of the PyC is made up of 4 Lorentzian curves.[25,26]. The peaks at 1350 cm^{-1} and 1580 cm^{-1} represent the D and G peak respectively.[5] The curve around 1332 cm^{-1} is believed to be due to diamond-like carbon structures.[27] Finally, the curve around 1500 cm^{-1} is thought to be a result of amorphous carbon structures left over from the cured phenolic resin.[27,28]

A common measure used to quantify the nanostructure of carbon materials is the graphitic crystallite size (L_a), which is calculated from the (100) and/or (110) peaks of the x-ray diffraction (XRD) pattern using the Scherrer equations.[29–31] Alternatively, this may be approximated using the intensity (I_G/I_D) and/or area (A_G/A_D) ratios of the G and D bands of the Raman spectrum.[5,6,32,33] These approximations can be split into two types, one that shows L_a increasing with the G/D ratio and one showing a decrease , by utilizing the previously proposed three stage model of the transformation of graphite into diamond-like tetrahedral amorphous carbon (see Fig. 2.3 for an illustration of the model).[5,6]

The three stages of the previously reported model consist of the following transformations:[5,6] (1) graphite → nanocrystalline (NC) graphite; (2) NC graphite → amorphous carbon (a-C); (3) a-C → tetrahedral amorphous carbon (ta-C). For the bulk of graphitic materials, including the synthesis of PyC from phenol-formaldehyde, the two most applicable stages are stages 1 and 2,[6,34] and each stage has a correlation of I_G/I_D and/or area A_G/A_D (they are sometimes used interchangeably in the literature) from Raman spectroscopy to L_a. For stage 1, which is most heavily studied, the widely accepted correlation is $L_a \propto A_G/A_D$.[5,6,32,33,35] However, for small values of L_a (large number of defects), the linear relationship proposed for stage 1 will eventually fail,[5,6,34] and previous studies proposed the use of $L_a \propto (A_G/A_D)^{-\frac{1}{2}}$ for $L_a \lesssim 3$ nm.[5,6,30] In this report, the stages (1 or 2) that most closely resemble microstructure of the PyCs made are determined.

2.2.2 Vickers Microhardness

High temperature processing enables the migration of defects in the graphitic crystallites that comprise the PyCs.[17] Thus, evaluation of the mechanical behavior of the PyCs as a function of pyrolyzation temperature (T_p) is required. The PyCs are highly porous,[1,36] making it necessary to evaluate the mechanical properties of the PyCs using a microscale indentation technique known as Vickers microhardness. Recent studies of the mechanical behavior of defective graphene indicates that the presence of lattice vacancies lead to reduced stiffness,[37–39] and that processing that shifts the microstructure of the PyCs from stage 2 to stage 1, such as higher T_p, will lead to significantly higher elastic moduli and breaking loads.[39]

Crystallite size, L_a , can be found using the following formulas (in units of nm) for an excitation wavelength $\lambda = 533$ nm:[5,32,33]

$$L_a = \frac{1}{4.4}\left(\frac{A_G}{A_D}\right) \tag{2.1a}$$

$$L_a = 2.4 \times 10^{-}10\lambda^4 \left(\frac{A_G}{A_D}\right) \tag{2.1b}$$

$$L_a = \frac{1}{0.55}\left(\frac{A_G}{A_D}\right)^{-\frac{1}{2}} \tag{2.1c}$$

These scaling relations proposed by Tuinstra and Koenig (Eq. 2.1a),[32] Cançado et al. (Eq. 2.1b),[33] and Ferrari and Robertson (Eq. 2.1c),[5] in conjunction with the L_a values approximated from XRD, will be considered. The optimal equation will be determined and used along with XRD analysis to determine which stage best describes the microstructure of the PyCs.

2.2.3 X-Ray Diffraction

X-ray diffraction (XRD) has long been used to analyze nanocrystalline materials.[7,15,40] An incident beam is scattered due to the crystalline atoms within the sample, and the detector is able to pick up the different angles at which the incident beam was scattered at. This collection of angles allows for an understanding of the electron density throughout the crystalline sample, which can then be used to find the positions of the atoms with regard to each other (diffraction pattern). Crystallite dimensions can be determined using the resulting diffraction pattern which, for our case, exhibit 2 peaks of interest for this study, the (002) and (100) peaks. These peaks are used to calculate the L_c and L_a crystallite sizes respectively. Fig. 2.4 shows the meaning of these crystallite sizes with respect to our sample.[7]

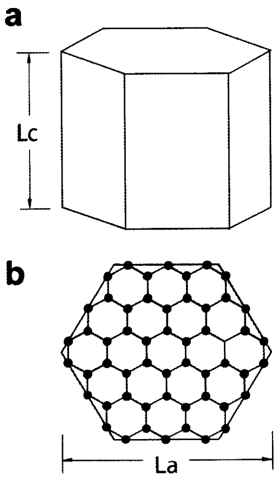

Figure 2.4: Schematic of crystallite shape showing (a) Lc and (b) La Image from Li et al.[7]

Chapter 3

Objectives and Approach

In this chapter, the general scope of this research will be discussed. The testing methods and why they were chosen will be described and discussed.

3.1 Objectives

The goal of this study is to further understanding how processing affects the structure and subsequent properties of the ceramic matrix. This study will delve into the processing parameter of temperature ramping rate (TRR). The temperature ramping rate will change how the phenolic resin pyrolyzes to form an amorphous carbon matrix, most likely through changing initial bonding and breaking of bonds, as well as changing how gases are formed and released. This will be analyzed and quantified using Raman Spectroscopy, XRD, and Vickers Microhardness Testing.

3.2 Approach

This study is broken up into three stages. Firstly, a brief look into the synthesis of PyCs, more specifically how the partial curing of the phenolic resin effects the subsequent pyrolyzed sample. This is followed by a more extensive investigation into morphology characterization, and finally mechanical characterization. Detailed approaches and motivations for the testing methods selected can be found in the remainder of this chapter while subsequent results can found in Chapter 5 and 6.

3.2.1 PyC Synthesis

The degree of cure of the phenolic resin before pyrolyzation is believed to have a significant influence on how the varying TRRs effect the overall bonding and cross-linking of the samples during the pyrolysis process. Unfortunately, this was not noted until late in the study, and as a result, this area of interest is only briefly discussed based on literature.

3.2.2 Morphology Characterization

XRD has long been a common way to quantify average crystallite sizes within materials. XRD will be used to confirm the trend of crystallite size (L_a and L_c) as a function of pyrolyzation temperature, as well as TRR. Confirming the trend between crystallite size and pyrolyzation temperature will allow for further and more concrete understanding of the pyrolyzation process for phenolic formaldehyde. Additionally, it will allow for a discussion on the reliability of commonly used equations, as mentioned in Chapter 2, to determine crystallite size, L_a, using Raman Spectroscopy.

Raman Spectroscopy is a common method of determining disorder within carbon materials. In this study, Raman will be used to determine disorder and L_a trends as a result of TRR by looking at how the ($A_\mathrm{G}/A_\mathrm{D}$) ratio changes. Unlike XRD, which gives an average crystallite size, Raman allows for seeing how disorder and crystallite size varies throughout the sample.

3.2.3 Mechanical Characterization

Vickers Microhardness testing will be used to determine the hardness as a function of TRR. Density will be acquired using an electronic digital caliper to determine volume and a scale to determine weight. This method of acquiring density is arguably unreliable, and as a result, the possible trends of specific hardness, which incorporates each sample's density when calculating, will be only briefly discussed. Vickers Microhardness testing shows if hardness varies over the sample's surface.

Chapter 4

Processing and Experimental Procedures

In this chapter, the methods of preparing and testing the specimen will be discussed. Images and discussion on analysis methods will also be discussed for each testing method, including a brief description of expected error.

4.1 PyC Synthesis

Durite SC-1008 Phenolic Resin was acquired from Momentive Performance Materials, Inc. The resin was first degassed for approximately 24 hours at room temperature at $\sim 26inHg$. After degassing, the phenolic was put into pre-made silicon molds and cured at 80°C under vacuum (again $\sim 26inHg$) for 4 hours and then at 80°C and ambient pressure for 8 hours. Te degree of cure was such that the phenolic was hardened enough to process into sizable samples. In order to accommodate the needs of the XRD instruments, which calls for very thin samples, the partially cured phenolic resin was cut into 1cm×1cm pieces with a thickness of about 1mm. The samples were then pyrolyzed at 1000°C in situ during the XRD scanning. This process resulted in 2 specimen, of ramp rates 10°C/min, 20°C/min, and 40°C/min each, 6 specimen total. The samples then were tested using Raman Spectroscopy. Finally, the samples were returned to the silicon molds and an epoxy adhesive was applied over the sample. The epoxy mold, after being removed from the silicon mold, allowed the specimen to be more easily sanded and polished for Vickers Microhardness testing. See Fig. 4.1 for further understanding of PyC processing steps.

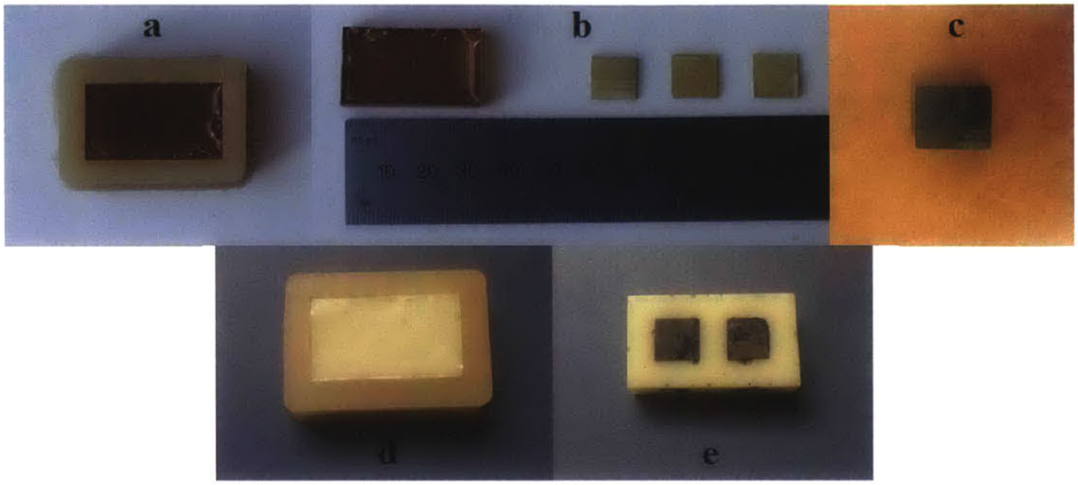

Figure 4.1: Image of sample preparation process. (a) cured phenolic resin in silicon mold, (b) cured phenolic outside of mold and pieces cut down and ready for pyrolysis, (c) example of pyrolyzed phenolic resin (older sample of larger size), (d) pyrolyzed pieces covered with epoxy in silicon mold, and (e) epoxy mold taken out of silicon mold after polishing.

4.2 Density

Between the in-situ XRD pyrolysis and Raman testing, the density of each specimen were calculated. Each specimen's weight was first measured using a Mettler Toledo scale, accurate to .001g. The volume was found using an electronic digital caliper, accurate to .01mm. The process of finding weight and volume was done 3 times per specimen. Due to the the difficulty in cutting/polishing to an perfect rectangular prism and the small size of the specimen, resulting calculated densities were somewhat reliable, but not exact enough to compare from specimen to specimen. This will be further discussed in Chapter 5.

4.3 X-Ray Diffraction (XRD)

The PANalytical X'Pert PRO XRPD was used for the XRD testing, and can be seen in Fig. 4.2. It has a 1.8kW sealed X-ray tube source, with a Cu target, and a vertical circle theta:theta goniometer with a radius of 240mm.

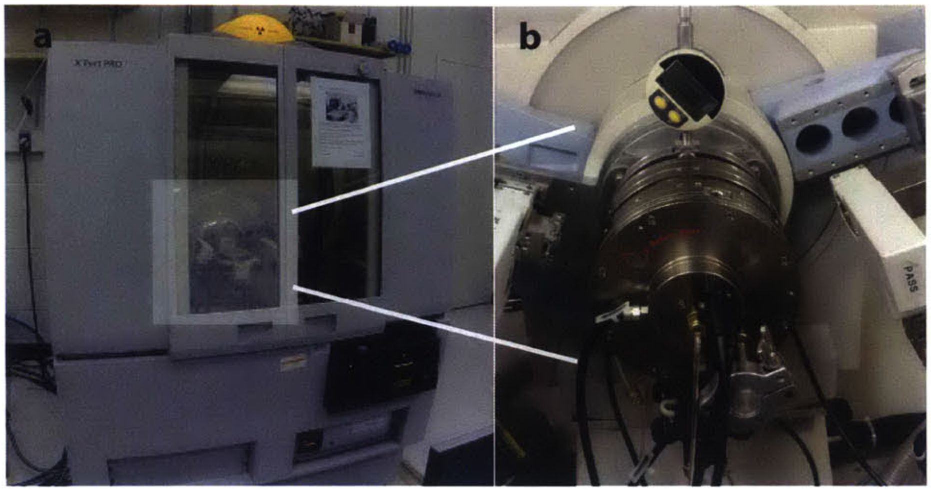

Figure 4.2: Image of (a) PANalytical X'Pert PRO XRPD and (b) a close up of the furnace attachment used.

Samples were individually loaded into the XRD furnace attachmentand tested at the required temperature ramping rate. The sample holder within the furnace was repositioned such that the top of the sample would be aligned with the x-ray beam. A program was set to take a 90 minute scan that scans the sample from 5 to 90 degrees using Bragg-Brentano geometry. A script was made for each temperature ramping rate, which first took a preliminary scan of the sample at room temperture (25°C), then ramped the temperature within the furnace to 1000°C at a given rate, stopping every 100°C between 600°C and 1000°C and performing the pre-written scan. After the final scan at 1000°C, the furnace would ramp down at it's highest rate of -50°C/min and take a final scan when the furnace and sample reached room temperature (25°C).

Analyzing of XRD spectra were done using HighScore Plus software(HS+). The spectra were converted from automatic divergence slit to fixed divergence slit data, the background was determined, and the Fit Profile function within HS+ was then used, allowing for the determination of the FWHM of the 200 and 110 peaks, used for the calculation of L_{c} and L_{a} respectively using the Scherrer Equation. Fig. 4.3 shows an example resultant spectra with and without background removed.

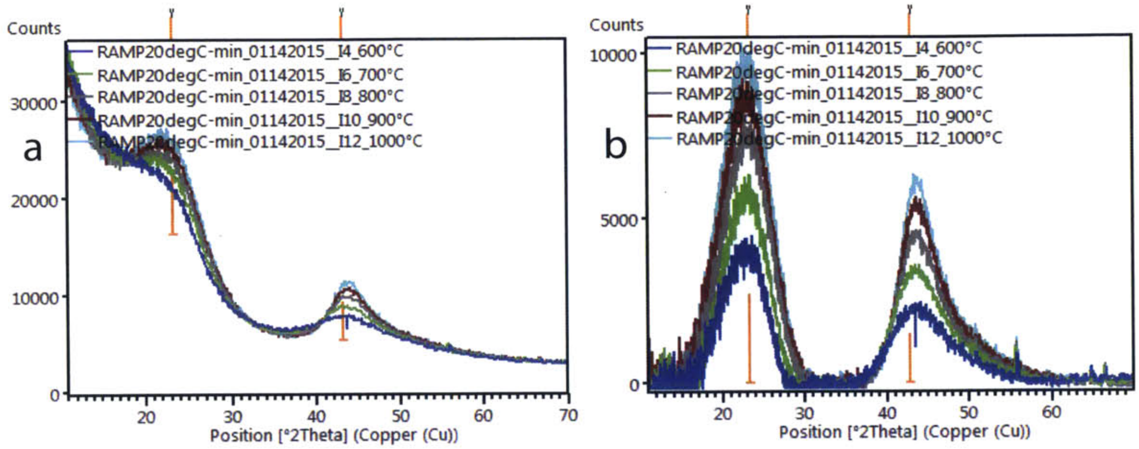

Figure 4.3: Resultant XRD spectra of 20°C/min TRR. (a) Spectra with background. (b) Spectra without background. 200 peak seen at $\sim 23^{\circ}$ and 110 peak seen at $\sim 43^{\circ}$

4.4 Raman Spectroscopy

During Raman spectroscopy, samples were positioned such that the laser beam hit the top of the PyC sample, closer to its center. A 533 nm laser wavelength, 50× objective magnification, and a time setting of two accumulations with each being 20 seconds were used. (See Fig. 4.4 for image of machine)

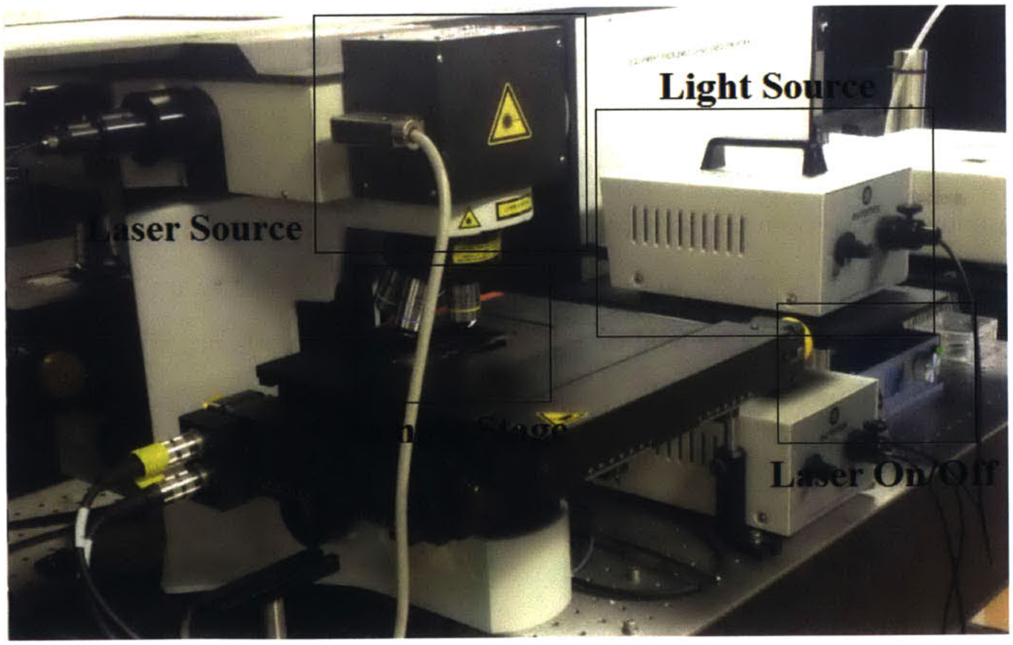

Figure 4.4: Image of Raman Machine.

At the beginning of the experiment, the laser was turned on and set to its Video setting, and the sample holder was moved carefully up and down to get to the appropriate working distance. The machine was then changed to Raman mode and a scan was taken. This process was done for several spots on each PyC sample to ensure that representative data was used when calculating the ratio of the integrated intensities of the G and D bands, or (A_G/A_D). These experimental parameters and procedure were utilized for all the Raman experiments discussed in this report. Crystallite size, L_a , was found using the Ferrari and Robertson equation[5] referenced in Chapter 2.

Due to limited software resources for analysis, the analysis of the Raman data was complex. The instrument gives a text document with intensity vs. Raman Shift. These text files were first normalized by the D peak to allow for easier comparison between scans, then the data file was put into the MATLAB cftool, which allows for approximate formula fitting. Four Lorentzian equations, as discussed in Chapter 2, were used to approximate the data, and the resulting formula was then put into a Mathematica script which plotted and integrated the spectra and output useful pieces of data such as G/D ratio, FWHMs, L_a, etc.

A sample spectra, and subsequent approximated formula plot can be seen in Fig. 4.5. The overlap in peaks was accounted for by only integrating the halves of the G and D peaks that were not overlapping (shaded regions). This method was also used to calculate the FWHM, which can be seen in red.

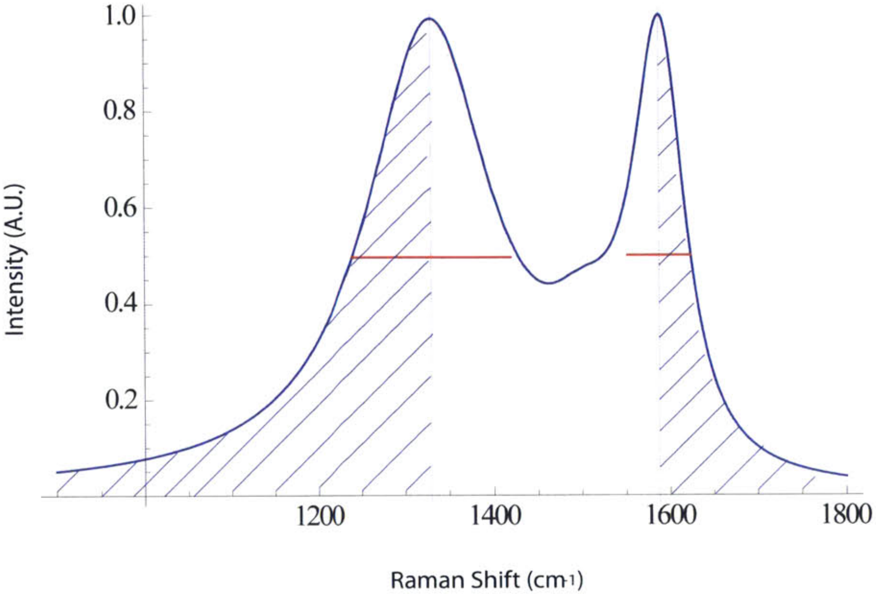

Figure 4.5: Schematic of typical spectra with FWHMs shown in red, and areas used to calculate G/D ratio shaded.

4.5 Vickers Hardness

A LECO LM Series Microhardness Tester, seen in Fig. 4.6, was used for Vickers Microhardness testing. Each mounted sample was placed under a 50× objective magnification lens. A force of 500 gf (≈ 4.9 N) was applied to each PyC specimen for 10sec. The Vickers machine gives the Vickers number (V) which is determined by the load applied and the resulting indentation surface area. The following relations can be used to calculate hardness (H_{V}) as well as specific hardness ($H_{\mathrm{V}}^{\star}$) in units of MPa using standard gravity (≈ 9.8), evaluated Vickers number (V), and apparent PyC density (ρ):

$$H_{\mathrm{V}} = 9.8V \tag{4.1a}$$

$$H_{\mathrm{V}}^{\star} = \frac{H_{\mathrm{V}}}{\rho} \tag{4.1b}$$

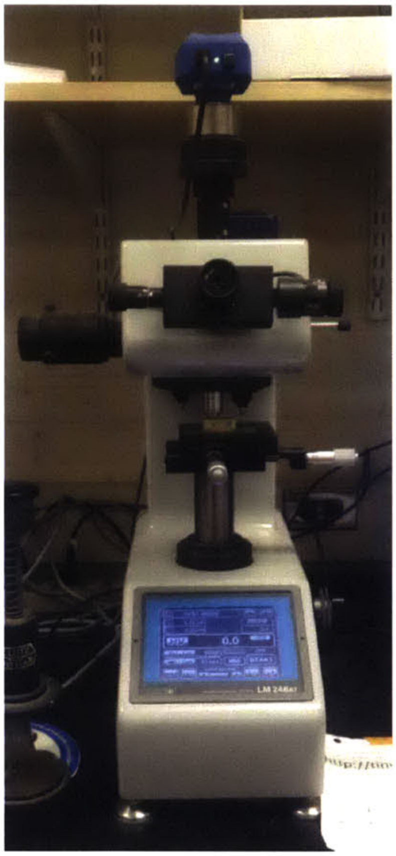
0.0
START
LM 248AT

Figure 4.6: Image of LECO Hardness Machine.

Chapter 5

Characterization

In this chapter, the results from XRD, Raman Spectrocopy, and Vickers testing will be discussed.

5.1 Morphology Characterization

From preliminary XRD and Raman Spectroscopy results, we see that weak trends show an increase in the prevalence of defects in the specimen as a result of increased TRR, resulting in slightly decreasing L_a values. Even results showing little to no trend are quite telling, implying that we are most likely in an interesting crystallite size range of 2-5nm for the PyC.

5.1.1 XRD Results/Discussion

Fig. 5.1 shows the evolution of L_a and L_c with respect to pyrolysis temperature for each TRR. See Table 5.1 for exact values of L_a. The main takeaways from these plots (which include standard error bars) is that there appears to be a decrease in crystallite size as a function of TRR. It is interesting to note that initial L_a at 600°C is almost the same for 10°C/min and 20°C/min TRR, while the final L_a at 1000°C is about the same for the 20°C/min and 40°C/min TRR. These relationships can be explained by thinking about gas production at lower and higher TRR's and temperatures.

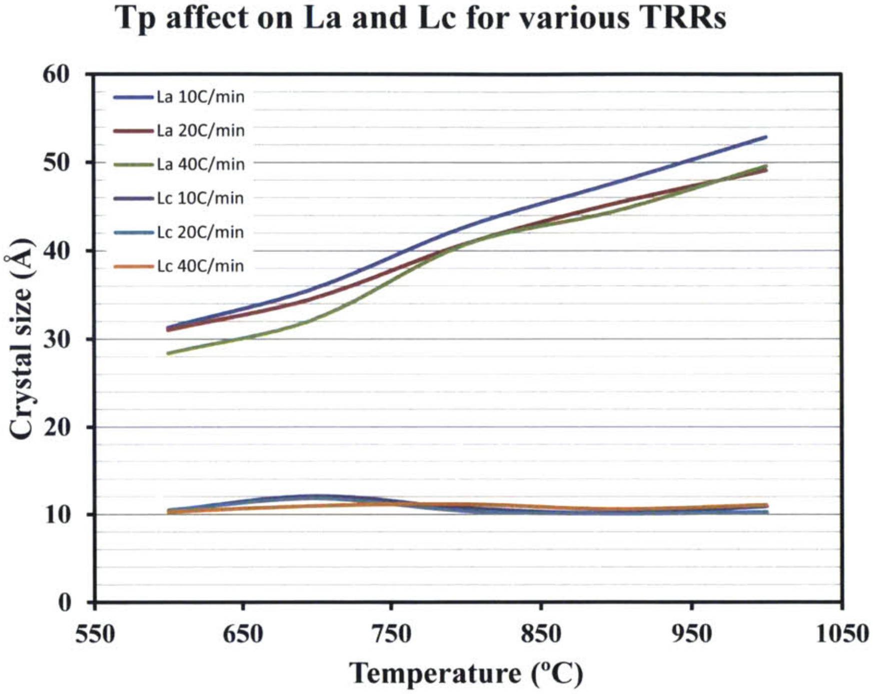

Figure 5.1: Plots of L_a and L_c values calculated from XRD analysis at varying temperature ramping rates.

Table 5.1: L_a (Angstroms) values for increasing Tp at varying TRRs

TRR	10°C/min	20°C/min	40°C/min
600°C	31.292	31.036	28.376
700°C	35.782	34.689	32.31
800°C	42.693	40.787	40.693
900°C	47.676	45.337	44.464
1000°C	52.867	49.088	49.569

Lower TRR: Gas Production and Cross-linking

The similarities between the lower TRR's are likely due to initial advanced curing. Recall that in Chapter 2, curing was described as happening in two stages, one at around 70°C, the other between 120°C and 150°C. Our samples are initially cured at 80°C, meaning they are never reaching the typical second curing stage and therefore are only partially cured when the in-situ pyrolyzation process takes place during XRD. At lower TRR's the sample has more time to be in the range leading up to and in stage 2. This means it has more time to form the cross-linking bonds previously described and is a more cured sample when pyrolysis begins.

Higher TRR: Gas Production and Structural Instability

The similar L_a size after reaching the 1000°C pyrolysis temperature at the higher TRR's are likely due to the increased instability of gas production. With gases being produced at a faster rate, there is less time for rebonding/cross-linking to occur in an orderly fashion. Additionally, the gases are trying to escape at a much faster rate, likely being the cause of micro-cracks found in some of the higher TRR samples.

It should also be noted that the rate at which L_a increases with respect to pyrolysis temperature (the slope) changes with TRR, though from initial studies and literature research, it not clear why. Also, L_c is not discussed, as how the carbon layers stacks is not as easily affected by an increase in disorder (or order), explaining why L_c is not significantly changing with respect to increasing TRR.

5.1.2 Raman Spectroscopy Results/Discussion

Fig. 5.2 and Fig. 5.3 show trends for FWHM of the G and D peak and L_a respectively. We see that the FWHMs of both peaks seem to be increasing, though the increase falls within the standard error of the various TRR's. L_a does not show a trend with respect to TRR. The lack of a clear trend in the L_a plot is most likely due to one of two reasons:

1.) **The crystallite size being around 2-5nm.** Using the Ferrari and Robertson equation resulted in an estimated L_a of 2-3nm. The 2-5nm size range has been discussed to be one of transition when it comes to the relationship between G/D ratio and crystallite

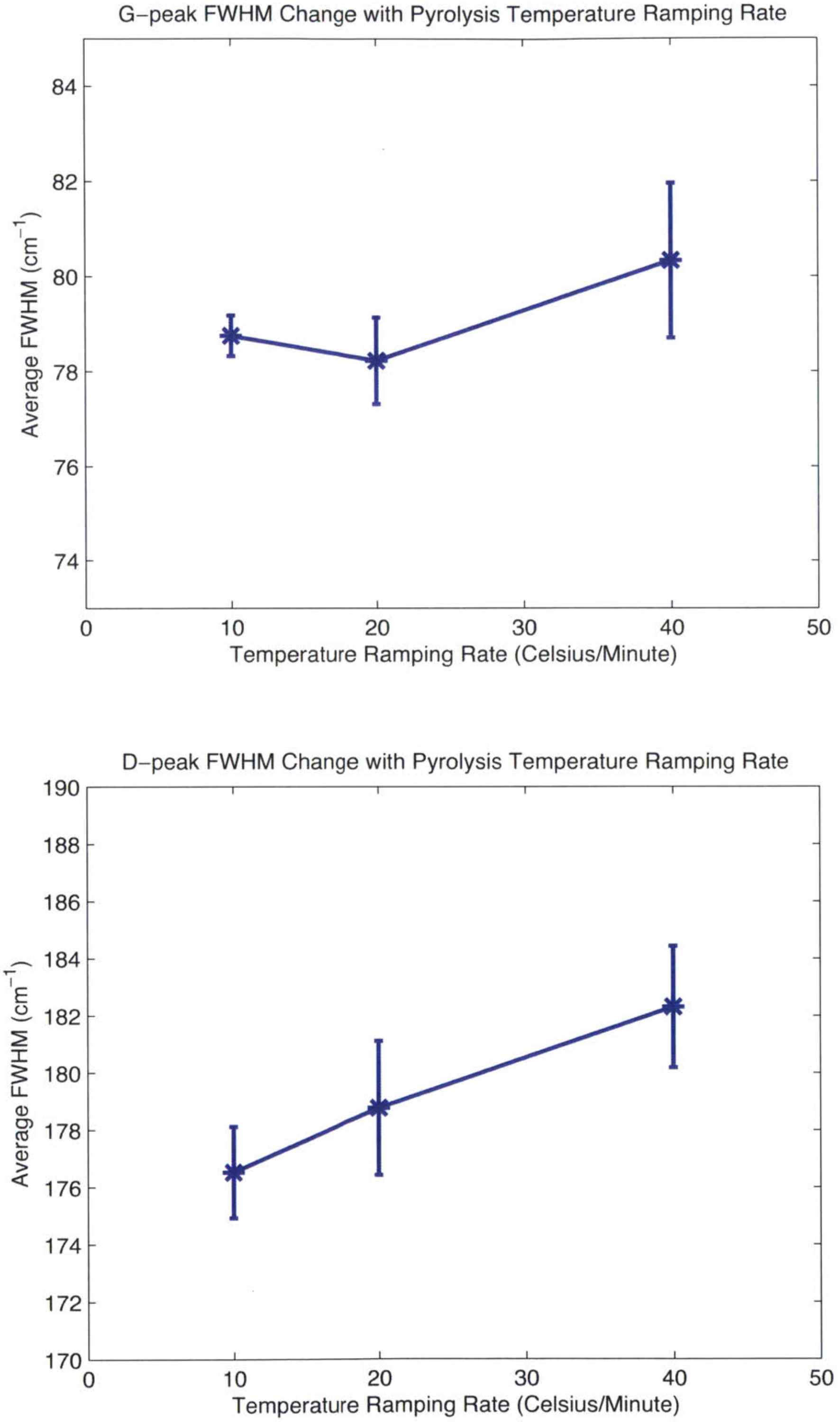

Figure 5.2: Plots showing (a.) G-peak FWHM and (b.) D-peak FWHM change with respect to TRR with standard error bars.

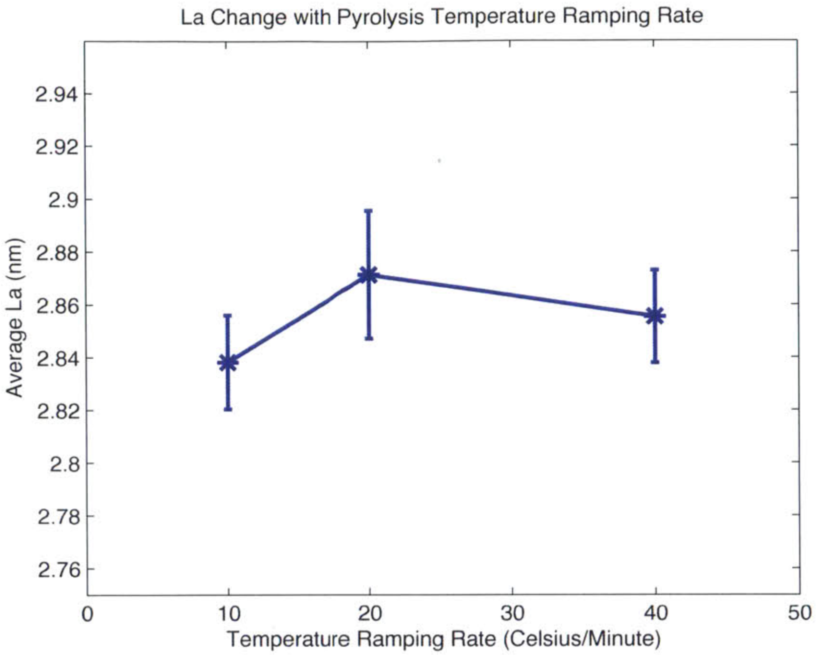

Figure 5.3: Plots showing La change with respect to TRR with standard error bars.

size.[8,26] In Fig. 5.4, which shows the two relations between L_a and G/D ratio converging at $\approx 2nm$ (or 20 Angstroms), Ferrari shows that relationship between G/D ratio and L_a size inverts and is therefore not reliable at certain crystallite sizes. This means that in the 2-5nm range, which is what has been calculated from XRD (an arguably more reliable source for crystallite size overall) it is difficult to gauge crystallite size from G/D ratio, as the relationship is somewhat flat as it transitions. XRD shows our L_a is closer to 5nm or 50 Angtroms. The significant disagreement between the L_a values given by XRD and Raman support the theory that the range of this transition may include L_a values around 5nm.

2.) **The analysis methods.** Due to the overlap between the D and G peak and, how broad the D peak is compared to the G-peak, part of the assumed G-peak's broadening was likely due to the overlap, even after correcting. With these two reasonings in mind, the trend of the D-peak plot is used to describe how the sample is affected.

Since we know broadening of the G and D-peak speak to an increase in disorder, we can infer that the trend of the D-peak corresponds with disorder increasing with increased TRR.[8] All of the plots also show a trend of increase in standard error with respect to TRR. This shows that the increased TRR is causing inhomogeneity within the sample.

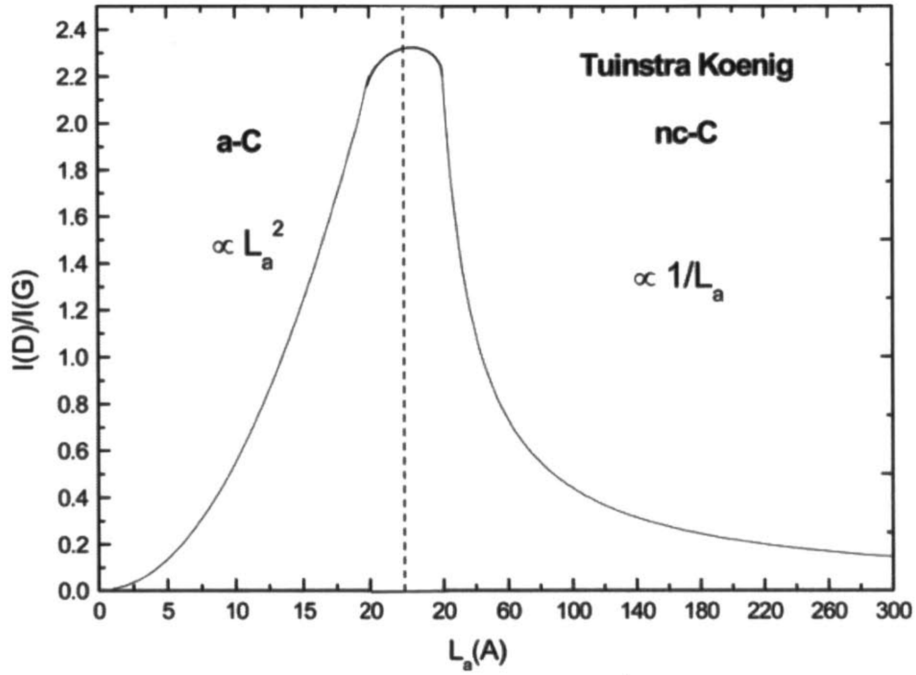

Figure 5.4: Plot showing evolution of (I_G/I_D) as a function of disorder. The maximum of the curve is representative of the transition between nanocrystalline graphite and amorphous carbons. Image taken from Ferrari et al. paper.[8]

This inhomogeneity can be explained in the same fashion as explaining decreased L_a size in the XRD discussion. Lower TRR makes for a more cross-linked cured phenolic resin, therefore a more homogenous sample to begin with pre-pyrolyzation. Lower TRR also result in slower gas production, allowing for slower, more stabile, reformation of cross-links, leading to a more homogenous system.

5.2 Hardness

Fig. 5.6 shows that hardness of the PyC stays relatively constant as a function of TRR. Again, it can be seen that the standard error increases quite dramatically at the higher TRR values. Using the same explanation as in XRD and Raman Spectroscopy discussions, we can understand this trend as well. The increased TRR is causing a more heterogeneously structured specimen.

Due to the small size and inexact rectangular prism shape of the specimen, the error from measuring technique and statistical error were substantial. A decrease in density is evident between 10°C/min and 20°C/min, however the trend becomes unclear due to error between 20°C/min and 40°C/min. Calculated values for density and error can be seen in Table 5.2 and are shown in Fig. 5.5. Hardness and Specific Hardness are compared in Fig. 5.6.

Table 5.2: Density values for varying TRRs with error calculations

TRR	10°C/min	20°C/min	40°C/min
Run 1	1.26677	1.19499	1.205769
Run 2	1.31064	1.24912	1.16575
Run 3	1.28895	1.19066	1.14572
System Error	.0137478	.0130436	.0127049
Standard Statistical Error	.012664	.018807	.017652
Averages	1.288787 ± 0.018692	1.21159 ± 0.022887	1.172413 ± 0.021749

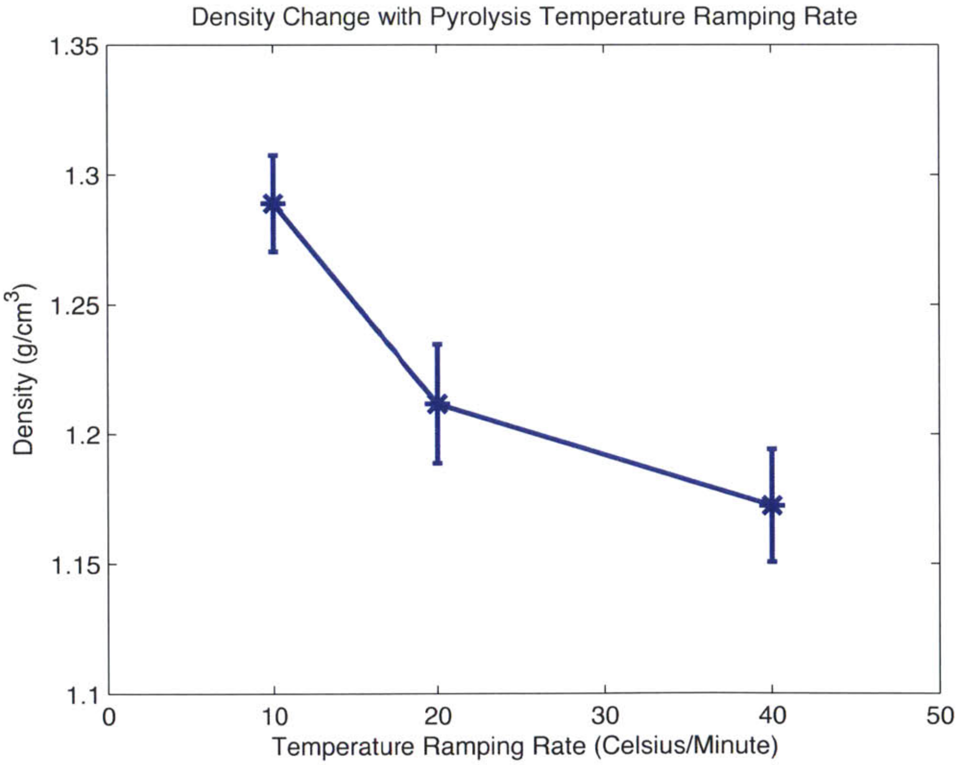

Figure 5.5: Plot showing density change with respect to TRR with standard/measured error bars.

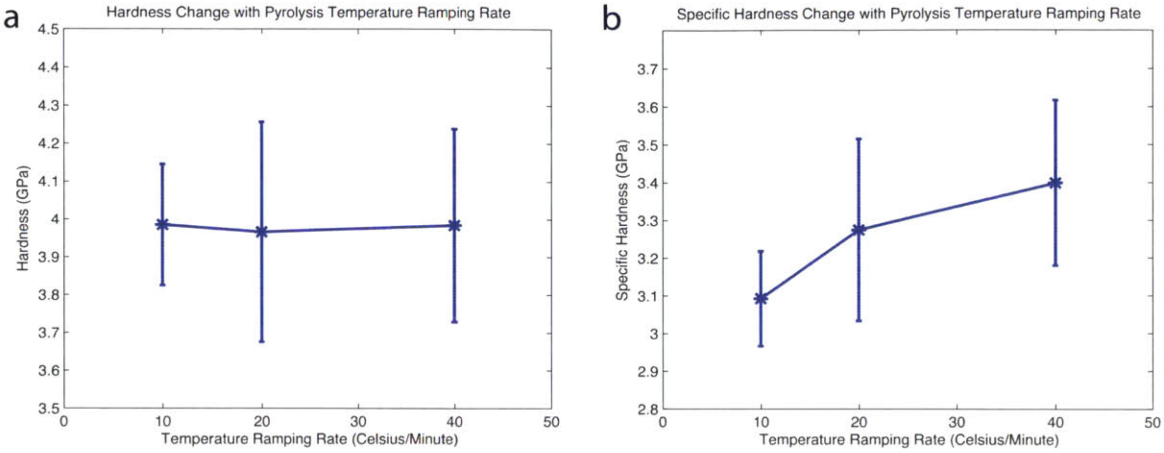

Figure 5.6: Plots showing (a) Hardness and (b) Specific Hardness changes with respect to TRR with standard error bars.

It can be seen that the error bars over shadow the trend that seems to be appearing. The porosity seems to be increasing with TRR, resulting in the heterogeneity of the hardness throughout the sample. From other testing analysis, it can be concluded that the porosity is also heterogeneous throughout the sample, with some spots maintaining the ideal density such as in the lower TRR specimen, leading to areas of seemingly high specific hardness, while others have higher porosity causing the overall density of the specimen to decrease.

Chapter 6

Conclusions and Recommendations

In this chapter, the conclusions drawn from our testing analysis and literature research as well as propose new processing parameters, specimen, and analysis techniques will be discussed.

6.1 Conclusions

The samples have an L_a size of $\sim$5nm, and trends in our data from Raman indicate the samples are in the transitional range from stage 1 to stage 2 described in Chapter 2. From XRD, it is seen that samples are decreasing in order resulting in smaller L_a caused by increased TRR, while L_c remains relatively constant. This is most likely a result of the increased TRR causing the partially cured phenolic resin to go though further curing/cross-linking before pyrolysis, resulting in a more cross-linked sample when the pyrolysis begins.

At lower pyrolyzation temperatures ($\lesssim$ 600°C) a TRR of 20°C/min or lower, allows the advanced curing to dominate the resulting structure of the sample. At higher pyrolyzation temperatures ($\geq$ 600°C) in combination with a 20°C/min TRR or higher, promotes unstable amounts of gas production to dominate the resulting structure of the sample. Gas production therefore is desired at slower rates of release but higher overall amounts (to some limit), and finding TRR's that take advantage of finding this balance throughout the curing/pyrolyzation process will result in both more highly ordered and homogenous PyCs.

Increasing TRR is also changing the slope at which L_a varies with respect to pyrolysis temperature (as seen in Fig. 5.1), but the reasoning behind this is currently unknown.

6.2 Future Work

6.2.1 Curing and XRD

The amount of cure is believed to have an effect on how the bonding, more specifically cross-linking, occurs and breaks down thus future studies should vary amount of cure while keeping other parameters constant. Looking at curing rates and their effects on the PyC using the in-situ XRD technique may have an effect on the resultant PyC bonding, but it appears the amount of cure would have a much more significant effect.

For XRD analysis, statistically significant data was not achievable due to time constraints. Future studies would have 2 or 3 runs per sample. Also, XRD showed that the scans taken at 1000°C were different from the scan taken after the sample cooled back down to room temperature. Both of these scans should represent a sample pyrolyzed to 1000°C, but produce different spectra, and most likely different crystallite sizes. Future studies should attempt getting the room temperature crystallite size for each pyrolysis temperature. Finally, since we see crystallite size growing with pyrolysis temperature and indirectly with TRR, looking into higher pyrolysis temperatures and lower TRR's are advised.

Studies to find the optimal TRR to use when curing/pyrolyzing up to around 600°C, and similarily when passing 600°C for higher temperature pyrolysis, would be highly efficient and beneficial. From this initial study, it is suggested to begin around 20°C/min, then decreasing to 10°C/min when passing 600°C.

6.2.2 Vickers Hardness Testing

Due to the discussion on gas production at higher TRR's, it was hypothesized that higher TRR's would result in lower densities. Owing to the samples being very thin to accommodate the needs of the XRD, calculate average values for density was not achieved without overlapping error bars. However, a trend of decreasing density does seem to exist. An in depth study into how of the Specific Hardness is changing with TRR is required thus larger samples will be made following the same pyrolysis procedure as the XRD samples to reduce measured error.

References

[1] I. Y. Stein, B. L. Wardle, *Carbon* **68**, 807 (2014).

[2] I. Stein, Synthesis and characterization of next-generation multifunctional material architectures : aligned carbon nanotube carbon matrix nanocomposites, Master's thesis, Massachusetts Institute of Technology (2013).

[3] J. Kane, N. Mowrer, Phenolic resin compositions with improved impact resistance (1996). WO Patent App. PCT/US1996/005,454.

[4] D.-e. Jiang, A. C. T. van Duin, W. A. Goddard, S. Dai, *The Journal of Physical Chemistry A* **113**, 6891 (2009).

[5] A. C. Ferrari, J. Robertson, *Phys. Rev. B* **61**, 14095 (2000).

[6] A. C. Ferrari, D. M. Basko, *Nat. Nanotechnol.* **8**, 235 (2013).

[7] Z. Li, C. Lu, Z. Xia, Y. Zhou, Z. Luo, *Carbon* **45**, 1686 (2007).

[8] A. C. Ferrari, *Solid State Communications* **143**, 47 (2007).

[9] M. F. L. De Volder, S. H. Tawfick, R. H. Baughman, A. J. Hart, *Science* **339**, 535 (2013).

[10] D. Kauffman, A. Star, *Angew. Chem., Int. Ed.* **47**, 6550 (2008).

[11] Q. Cao, J. A. Rogers, *Adv. Mater.* **21**, 29 (2009).

[12] L. Liu, W. Ma, Z. Zhang, *Small* **7**, 1504 (2011).

[13] L. An, *et al.*, *Adv. Mater.* **16**, 2036 (2004).

[14] S. Sarkar, *et al.*, *ACS Appl. Mater. Interfaces* **2**, 1150 (2010).

[15] X. Li, K. Li, H. Li, J. Wei, C. Wang, *Carbon* **45**, 1662 (2007).

[16] D. Bansal, S. Pillay, U. Vaidya, *Carbon* **55**, 233 (2013).

[17] C. D. Latham, M. I. Heggie, M. Alatalo, S. Öberg, P. R. Briddon, *J. Phys.: Condens. Matter* **25**, 135403 (2013).

[18] T. Trevethan, *et al.*, *Phys. Rev. Lett.* **111**, 095501 (2013).

[19] M. S. Dresselhaus, A. Jorio, M. Hofmann, G. Dresselhaus, R. Saito, *Nano Lett.* **10**, 751 (2010).

[20] A. V. Krasheninnikov, K. Nordlund, *J. Appl. Phys.* **107**, 071301 (2010).

[21] M. G. Kim, W. L. S. Nieh, R. M. Meacham, *Ind. Eng. Chem. Res.* **30**, 798 (1991).

[22] J. Wang, H. Jiang, N. Jiang, *Thermochimica Acta* **496**, 136 (2009).

[23] S. Curran, J. Talla, D. Zhang, D. Carroll, *J. Mater. Res.* **20**, 3368 (2005).

[24] M. Dresselhaus, G. Dresselhaus, R. Saito, A. Jorio, *Phys. Rep.* **409**, 47 (2005).

[25] P. Mallet-Ladeira, *et al.*, *Carbon* **80**, 629 (2014).

[26] P. Mallet-Ladeira, P. Puech, P. Weisbecker, G. L. Vignoles, M. Monthioux, *Applied Physics A* **114**, 759 (2013).

[27] J. Schwan, S. Ulrich, V. Batori, H. Ehrhardt, S. R. P. Silva, *Journal of Applied Physics* **80**, 440 (1996).

[28] S. Prawer, K. Nugent, D. Jamieson, *Diamond and Related Materials* **7**, 106 (1998).

[29] N. Iwashita, C. R. Park, H. Fujimoto, M. Shiraishi, M. Inagaki, *Carbon* **42**, 701 (2004).

[30] G. A. Zickler, B. Smarsly, N. Gierlinger, H. Peterlik, O. Paris, *Carbon* **44**, 3239 (2006).

[31] H. Badenhorst, *Carbon* **66**, 674 (2014).

[32] F. Tuinstra, J. L. Koenig, *J. Chem. Phys.* **53**, 1126 (1970).

[33] L. G. Cançado, *et al.*, *Appl. Phys. Lett.* **88**, 163106 (2006).

[34] L. G. Cançado, *et al.*, *Nano Lett.* **11**, 3190 (2011).

[35] M. Lucchese, *et al.*, *Carbon* **48**, 1592 (2010).

[36] I. Y. Stein, H. M. Vincent, S. A. Steiner, E. Colombini, B. L. Wardle, *54th AIAA Structures, Structural Dynamics, and Materials (SDM) Conference* (Boston, MA, 2013).

[37] R. Dettori, E. Cadelano, L. Colombo, *J. Phys.: Condens. Matter* **24**, 104020 (2012).

[38] M. Wang, C. Yan, L. Ma, N. Hu, M. Chen, *Comput. Marter. Sci.* **54**, 236 (2012).

[39] A. Zandiatashbar, *et al.*, *Nat. Commun.* **5**, (2014).

[40] A. K. B. Manoj, *Int. J. Electrochem. Sci.* **7**, 3127 (2012).